Mechanistic insights into photogenerated electrons store-and-discharge in hydrogenated glucose template synthesized Pt: TiO_2/WO_3 photocatalyst for the round-the-clock decomposition of methanol

Maryam Mokhtarifar [1,2], Duc Trung Nguyen [1], Mohan Sakar [3,] MariaPia Pedeferri [2], Marco Asa [4], Reyhaneh Kaveh [5],Maria Vittoria Diamanti [2*], and Trong-On Do [1*]

[1] *Chemical Engineering Department, Laval University, Quebec City, Canada*

[2] *Department of Chemistry, Materials and Chemical Engineering "G. Natta," Politecnico di Milano, Milan, Italy*

[3] *Centre for Nano and Material Sciences, Jain University, Karnataka, India*

[4] *Department of Physics, Politecnico di Milano, Milan, Italy*

[5] *Department of Chemistry, Sharif University of Technology, Tehran, Iran*

** Corresponding authors: mariavittoria.diamanti@polimi.it, trong-on.do@gch.ulaval.ca*

Abstract

This study demonstrates the glucose-template assisted synthesis of hydrogen-treated Pt: TiO_2/WO_3 composites, and their round-the-clock photoactivity towards methanol (MeOH) degradation under light illumination and in dark. XRD indicated increasing rutile fraction in TiO_2 as a function of template removal, WO_3 crystallinity and H_2 treatment process. The presence of oxygen vacancies in WO_3 was confirmed by XPS. Lower recombination rate and higher surface area were observed in the optimized H_2-Pt-G:TiO_2/WO_3 catalyst. The presence of oxygen vacancies and optical enhancements due to the synergistic interactions of the multi-system (TiO_2, WO_3 and Pt) extended the visible light absorption of the system, increasing photocatalytic activity, with 61% of MeOH degradation in 2 h of irradiation and 33% in dark in 6 h. The origin of the observed efficiency was further validated using photo-electrochemical investigations, which revealed appropriate interfacial contacts in Pt: TiO_2/WO_3 system, maximum charge separation and charge transfer thanks to oxygen vacancies.

Keywords: Round-the-clock photocatalysts, TiO_2, WO_3, Co-catalyst, Hydrogen treatment

1. Introduction

It could be argued that the redox reaction of common photocatalyst (PCs) such as TiO_2, occurs only under light illumination [1–3]. Therefore, its photocatalytic activity is generally quenched once the light illumination is turned off. To enhance the performance, catalytic reactions should be independent of photons and improved for their activity round-the-clock under both light irradiation and dark conditions. This type of PCs, namely round-the-clock PCs (RPCs), has recently received enormous interests in many photocatalytic applications including heavy metal ion removal, degradation of organic pollutants, and hydrogen production [4–6]. In this phenomenon, a portion of the photoinduced electrons in a PC will be stored in an electron storage material (ESM) under light illumination and then these stored electrons get released once the light is turned off [7–9]. Several implications should be noted in developing a RPC; first, the conduction band (CB) of the PC should be above of the CB edge of the ESM to ease the electron transfer from the PC to ESM. Second, an adequate coupling is required between the PC and ESM to facilitate the electron transfer. Moreover, the ESM should release electrons slowly in dark to the PC to continue the catalytic reactions in dark. As an ESM, the WO_3 has been coupled with TiO_2 as an effort to develop TiO_2/WO_3-based RPC [10]. However, the conventional methods to prepare TiO_2/WO_3 heterostructure cause some restrictions in electron charge and discharge capacities, which is essentially due to the minimal contact at the interface of TiO_2/WO_3 [4,11]. Therefore, the photoactivity of TiO_2/WO_3 RPC was limited under UV light along with an undesirable electron charge-discharge performances [7,12].

To overcome such drawbacks, strategies such as defect engineering through H_2 treatment and templating approaches can induce the structural changes in TiO_2, WO_3 or both [11,13]. Among different types of defects, oxygen vacancies have been employed to induce both chemical and physical defects in the structures of the oxides [14]. These oxygen vacancies in TiO_2/WO_3 system could act as photoinduced charge traps, enhance photoabsorption and electron storage ability, thereby boosting the performances of RPCs [11,13,15–20]. For instance, in the case of WO_3, new structural features are formed through oxygen vacancies, consisting of different octahedral blocks of $[WO_6]$, where their corners are being shared regularly by the defect planes [19–24]. On the other hand, it is well known that the glucose, which is an inexpensive and non-toxic hard template, can serve for the synthesis of materials with higher surface area and can be removed easily through

thermal decomposition by heating it above 150 ºC [25–28]. Furthermore, glucose could act as a stabilizer to enhance the TiO_2 anatase formation through the presence of open chain aldehyde (as isomeric structure of glucose), acting as the oxygen-supplying agent in formation of anatase crystalline phase [29].

Apart from the defect engineering approaches, the use of metallic cocatalyst nanoparticles (NPs) is another technique to achieve the enhancements in the RPCs [11,30–35]. In this direction, Ni, Ag, and Pt NPs can enhance the performance of RPCs by harvesting the visible light through the surface plasmon resonance and also accepting the stored electron from ESM (thus enhancing charge separation)[11,30]. Notably, Pt is considered as the preferred metallic NP for oxygen activation in catalyzing reactions and it can be loaded on the RPC such as TiO_2/WO_3 heterostructures [36,37].

Though WO_3/TiO_2 based photocatalysts is the subject of considerable number of works [36–39], only few of them have examined its electron storing capacity to continue the catalytic activity after switching off the light. For instance, Khan et al. [40] (2019) and Park et al. [41] (2020) reported TiO_2/WO_3 based structures which can store electrons for *ca.* 2 h and 5 h, respectively. In order to take more advantage from such beneficial properties and extend the photocatalytic activity time in dark, a template-mediated synthesis of TiO_2/WO_3 RPC was developed in this work. The structure of this RPC is further modified by glucose templated approach and H_2 treatment process to induce oxygen vacancies and by decorating with the Pt NPs. Herein, a ternary heterostructure with high surface area has been formed and the Pt metal NPs, as a co-catalyst, were uniformly loaded onto the surface. This structure has manifested the unique properties including high sunlight absorption and charge separation, and sufficient electron storage capacities.

2. Material syntheses

2.1 Chemicals

D -(+)-Glucose, titanium isopropoxide (TTIP), hexachloride tungstate (WCl_6), hydrogen peroxide (H_2O_2), ethanol (EtOH), and chloroplatinic acid (H_2PtCl_6) were purchased from Sigma-Aldrich. High Pt-H_2 treated glucose templated TiO_2/WO_3 was prepared via a multistep pathways (Fig.1) consist of the following steps: (i) glucose templated synthesis of TiO_2/WO_3 (G:TiO_2/WO_3); (ii) H_2 treatment of G:TiO_2/WO_3 to obtain a defective structure (H_2-G:TiO_2/WO_3); (iii) Pt loading on H_2-G:TiO_2/WO_3.

2.2 Synthesis of glucose templated TiO_2/WO_3 (G: TiO_2/WO_3)

Three stock solutions were prepared as followed. Solution I was obtained by dissolving 17 g D-(+)-Glucose in 150 mL distilled water with stirring for 10 min. Solution II was obtained by adding 1 g Titanium isopropoxide (TTIP) dropwise to a mixture of H_2O_2 30 wt.% (7 g) and 43 g distilled water under stirring for 10 min. Solution III was obtained by dissolving an appropriate amount of WCl_6 in 50 ml absolute EtOH. At the beginning, the color of solution III gradually changed from yellow to colorless as the replacement of the chlorine ions in WCl_6 by the ethoxide groups completed. Finally, solution III turned to dark blue, indicating the formation of amorphous $WO_3 \cdot nH_2O$. To synthesize G: TiO_2/WO_3, three stock solutions were mixed homogeneously under stirring for 4 h, followed by drying at 80-100 ^oC. The obtained solid was subjected to one-step calcination at 550 °C for 5 h (heating air rate of 5 $^oC.\ min^{-1}$) to form the crystalline phase of the material as well as to remove the template. The prepared sample (with a TiO_2:WO_3 ratio of 80:20) was named G:TiO_2/WO_3.

2.3 Synthesis of H_2-treated G:TiO_2/WO_3 (H_2-G:TiO_2/WO_3)

100 mg G:TiO_2/WO_3 powder was treated in a tube furnace at 400 °C at a hydrogen flow rate 200 mL. min^{-1} for 4 h. The obtained sample with enhanced oxygen vacancies and high surface area was denoted as H_2-G:TiO_2/WO_3.

2.4 Pt loading on H_2-G:TiO_2/WO_3 (H_2-Pt-G:TiO_2/WO_3)

Pt was deposited on H_2-G:TiO_2/WO_3 by photodeposition method. In a typical procedure, 100 mg of H_2-G:TiO_2/WO_3 was dispersed in 200 mL methanol. Then, 1.5 wt% aqueous solution of H_2PtCl_6 was added. The mixture was irradiated by a solar simulator 150 W Xe lamp (AM 1.5 G, 100 mW cm^2) (without an optical filter) for 6 h. The initial milky white suspension turned to light grayish color, indicating the deposition of Pt nanoparticles. The resultant H_2-Pt-G:TiO_2/WO_3 composites were retrieved by centrifugation at 6000 rpm, and then washed five times with excess methanol and dried under vacuum(**Figure 1**).

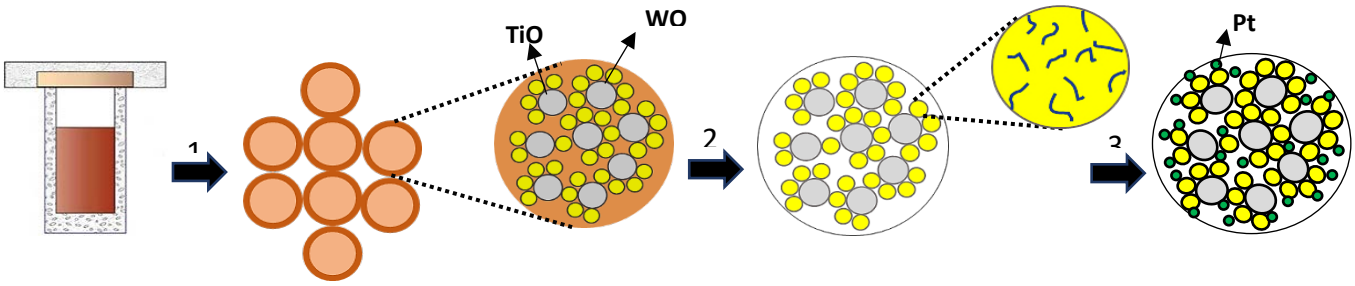

Figure 1. Schematical synthesis of H_2 -Pt-G:TiO_2/WO_3 nanospheres: (1) one-pot synthesis of glucose templated TiO_2/WO_3, (2) calcination of G:TiO_2/WO_3 at 550 °C for 5 h followed with H_2 treatment at 400 °C for 4 h, and (3) loading of Pt nanoparticles cocatalyst on H_2 - G:TiO_2/WO_3.

2.5 Characterizations

All the materials were characterized using BET specific surface area analysis, X-ray diffraction (XRD) technique, UV–Visible spectroscopy (UV–Vis), Photoluminescence (PL) measurements, X-ray photoelectron spectroscopy (XPS), electrochemical measurements and photodegradation tests to understand their various characteristics such as morphology, crystal/chemical structure, optical properties and photocatalytic performances. In specific, the nitrogen adsorption/desorption isotherms were measured at 77 K on an ASAP 2020 (Micromeritics Instrument Corp., Norcross, GA, USA). All the products were degassed in vacuum at 150 °C for 8 h before BET measurements. X-ray diffraction (XRD) patterns were done on the dried powders at the scanning rate of 2.5°/ min with Cu $K_{\alpha 1}$ radiation (2θ range 20-60°) on a Philips PW1830 powder diffractometer (40 kV voltage and 40 mA filament current). The anatase and rutile weight fraction with respect to the whole amount of TiO_2 crystalline phases (anatase, rutile) was calculated according to Eq. 1[42] (I_R and I_A are the intensities of (110)rutile and (101)anatase reflections).

$$f_A = \frac{1}{\left(1 + 1.26\frac{(I_R)}{(I_A)}\right)}\% \qquad \text{Eq. 1}$$

Raman spectra were recorded with a LABRAMHR800 equipped with a Peltier cooled CCD detector at λ = 514 nm excitation by an argon ion laser (Stabilite 2017, Spectra Physics). UV-Vis absorption was measured with a Cary 300 Bio UV-Vis spectrophotometer. X-ray photoelectron spectroscopy (XPS)(Kratos Axis Ultra) was done in a light source of X-ray (Al Kα; hν = 1486.6

eV), and internal calibration was done in the C peak located at 285.0 eV . Photoluminescence (PL) measurements were performed using CARY ECLIPSE.

2.6 Photoelectrochemical characterizations

The working electrodes were prepared by drop-casting technique [43]. In a typical procedure, to prepare a homogeneous solution, the photocatalyst (20 mg) was dispersed in water (5 mL), the solution was sonicated and then drop-casted onto a FTO glass (2 cm^2)and dried at 80 °C for 24 h. The photocurrent response was recorded on a three-electrode configuration being the as-prepared electrode (TiO_2, G:TiO_2/WO_3, and H_2 -Pt-G:TiO_2/WO_3), Pt wire electrode, and silver/silver chloride (Ag/AgCl) as working, counter and reference electrode, respectively. All the electrochemical measurements were performed using a potentiostat (EG&G 263A2) instrument. To evaluate photocurrent response, as difference of current density between illumination and dark, the working electrode was polarized at 0.8 V *vs.* Ag/AgCl in dark and chopped light irradiation (10 s duration) with a source of solar light (150 W Xe lamp). Photocurrent was evaluated as difference of current density response between illumination and dark. The electrochemical impedance and Mott-Schottky plots were also recorded by the same system with a frequency between 100 KHz to 100 mHz and a frequency of 1 kHz in the range of -1.5 to +0.8 V (vs. Ag/AgCl), respectively. Open circuit potential measurements were also done in dark and under irradiation.

2.7 Photocatalytic methanol decomposition

The photo-oxidation of methanol (MeOH) was performed in an open system under a solar simulator (Abet model, 150 W Xe lamp, AM 1.5G, 100 mW/cm^2).A 100 mg of photocatalyst was dispersed into a 400-ppm aqueous MeOH solution (200 g). The system was then illuminated for 2 h under solar light to characterize the photocatalytic activity of the glucose-templated TiO_2/WO_3 nanocomposites with varying loading of WO_3. The non-decomposed methanol was detected using a gas chromatograph, and MeOH concentration was calculated as following.

$$C = C_0 * {}^{\text{remaining moles of MeOH}}/_{\text{initial moles of MeOH}}$$

The decomposition of MeOH with regular intervals of time during photo-irradiation was calculated by plotting ($(C_o\text{-}C)/C_o)*100$). The kinetics of decomposition of methanol in presence of the photocatalysts after gaining the adsorption-desorption equilibrium in dark (20 min) was calculated in the following for five selected samples as example of all calculations. It was observed that all the samples exhibit pseudo-first-order kinetics of photo-oxidation ($ln(C/C_0) = -K_{app}\, t$) [44,45].

3. Results and Discussion

The XPS and SEM analyses were done to study the chemical composition and morphology of the samples. The XPS survey spectrum of H_2-Pt-G:TiO_2/WO_3 confirmed the presence of Pt, W, Ti, O, and their native oxidation states, as displayed in **Figure 2**.

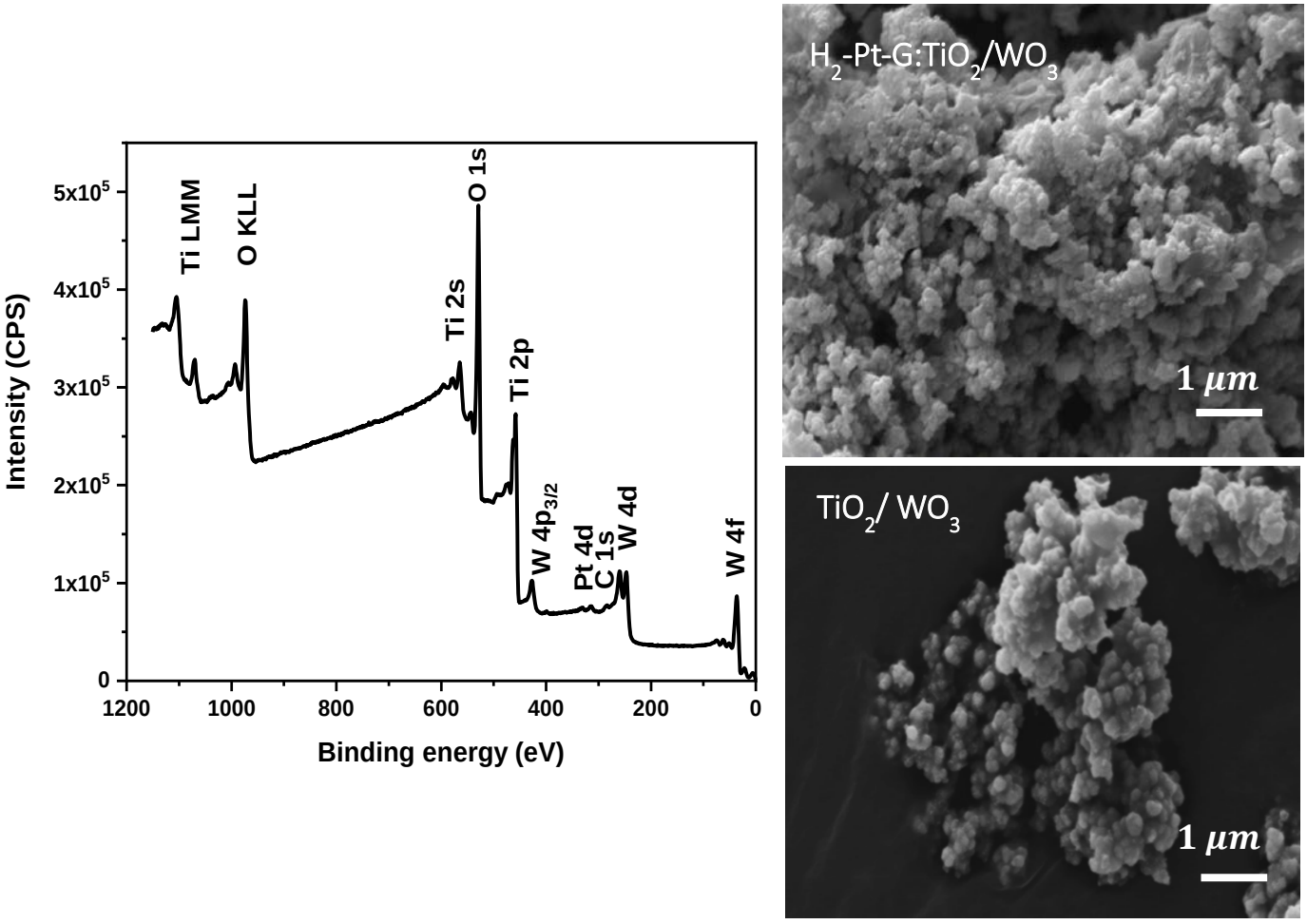

Figure 2. XPS survey spectra of H_2-Pt-G:TiO_2/WO_3 and SEM images of H_2-Pt-G:TiO_2/WO_3(A) and G:TiO_2/WO_3 RPCs.

The morphology of G:TiO_2/WO_3 and H_2-Pt-G:TiO_2/WO_3 is found to be agglomerated near-spherical particles with average size of 400 and 200 nm, respectively. Notably, the agglomeration among H_2-Pt-G:TiO_2/WO_3 particles is found to be increased as compared to G:TiO_2/WO_3, which could be related to their relatively increased surface area due to their reduced particle size. These results confirm that the process of H_2 treatment and Pt deposition considerably modify the surface properties of the system, which could be ascribed to the creation of oxygen vacancies and more number of reaction sites on the surface of H_2-Pt-G:TiO_2/WO_3 particles.

Figure 3 and **Table 1** show the SEM-EDS elemental mappings and mass contribution of Ti, O, W, and Pt nanoparticles in the H_2-Pt-G:TiO_2/WO_3 RPC. It clearly shows presence and homogeneous distribution of these elements.

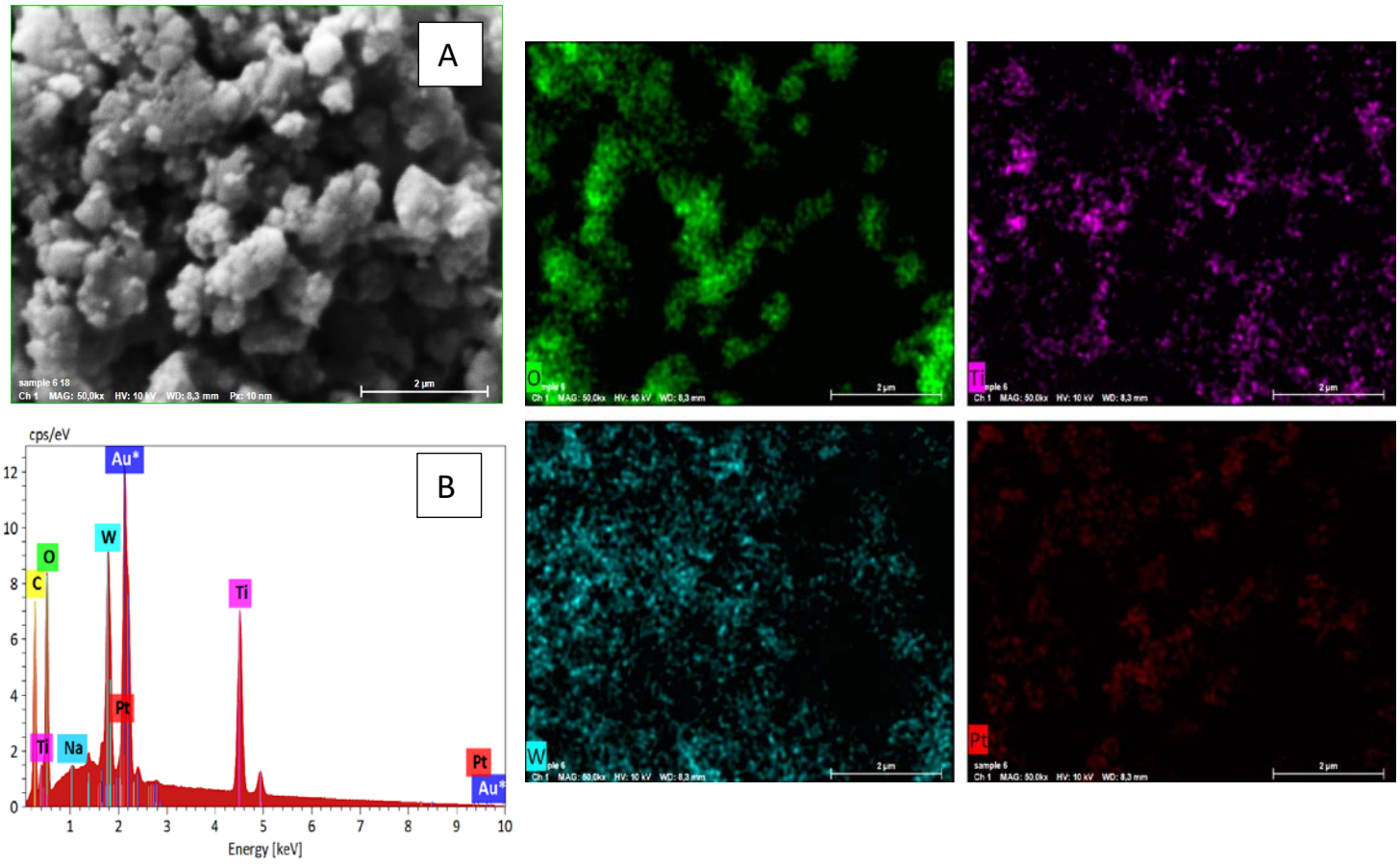

Figure 3 A) SEM image and B) EDS elemental mappings (B) of Ti, O, W, and Pt in H_2-Pt-G:TiO_2/WO_3 RPC (the presence of Au is due to surface gilding for SEM analyses, Na and C are present as impurities).

Table 1: Chemical composition of H_2-Pt-G:TiO_2/WO_3 RPC based on EDS data.

Element	Normalized mass (%)	Error (%)	At (%)
Titanium	32.77	3.53	20.4
Oxygen	21.50	11.03	40.06
Platinum	16.89	3.99	2.58
Tungsten	14.91	4.33	2.42
Carbon	13.92	11.3	34.54
SUM	100		100

Figure 4a displays the XRD pattern of bare TiO_2, G:TiO_2/WO_3 and H_2-Pt-G:TiO_2/WO_3 RPC. All the diffraction peaks are well matched to the standard diffraction pattern of biphasic anatase and rutile TiO_2 (JCPDS file No. 21-1272) (JCPDS file No. 21-1276) and WO_3 phase (JCPDS file No. 75-2187) [46], indicating that the present synthesis process successfully led to the formation of G:TiO_2/WO_3 heterostructures with high crystallinity. No peaks corresponding to Pt were detected by XRD due to their low concentration and high dispersion in H_2-Pt-G:TiO_2/WO_3 RPC [47].

The diffraction peaks at 25.5° and 27.4° can be assigned to (101), and (110) crystal planes of anatase and rutile TiO_2, respectively [48,49]. The concentration of anatase and rutile phase TiO_2 was estimated from its respective XRD peak using the following equation: $\chi = (1 + 0.8\, I_A/I_R)^{-1}$ [50,51]. Accordingly, the rutile content of in TiO_2, G:TiO_2/WO_3 and H_2-Pt-G:TiO_2/WO_3 was estimated to be 7, 20, and 29%, respectively. The increased rutile content in G:TiO_2/WO_3 and H_2-Pt-G:TiO_2/WO_3 could be originated due to the thermal process during the template removal, formation of crystalline WO_3 and H_2 treatment of the sample [39,52–56]. Furthermore, the XRD results also showed that the formation of WO_3 phase is pronounced in the H_2-Pt-G:TiO_2/WO_3 RPC, matching with the tetragonal phase with peaks at 23.1 °, 24.3 ° and 26.7 ° corresponding to (002), (020), and (200) planes, respectively [57]. While, it is well known that tetragonal phase in WO_3 almost appear in T > 740 °C [58–60], but the tetragonal WO_3 formation could be related to nanocrystalline properties of the different samples prepared by various methods [61–63] affecting by the thermodynamic conditions, which could make stable tetragonal WO_3 even at normal conditions. Overall, the pronounced peaks corresponding to TiO_2 and WO_3 phase clearly indicated the characteristic existence of these materials in H_2-Pt-G:TiO_2/WO_3, which remained unaffected through the processes such as template removal and Pt deposition, except the formation of defects

in the systems. These interesting features expected to positively influence the properties of the system [58,59,60].

The Raman spectra of the TiO_2, G:TiO_2/WO_3 and H_2-Pt-G:TiO_2/WO_3 samples are presented in **Figure 4b**. The presence of bands at about 145, 393, 516, and 640 cm^{-1} is attributed to the anatase TiO_2, while the peak at 446 cm^{-1} could be assigned to rutile phase. Furthermore, the bands at 275, 717.8, and 807.3 cm^{-1} could be attributed to WO_3 phase. The profiles of peaks such as intensity and their positions are relatively influenced by the subsequent modifications with the incorporation of WO_3, H_2 treatment and Pt deposition, which are in well-agreement with its respective discussion from the XRD results. For instance, the observed shift in the peak corresponding to TiO_2 in H_2-Pt-G:TiO_2/WO_3 with respect to bare-TiO_2 could be attributed to the reduced crystallite size [56] and defects-mediated structural changes in TiO_2 [57,58]. These defects may act as traps for the charge carriers and increase the photoactivity of the material to a greater extent[59].

The UV-visible absorption spectra of the synthesized TiO_2, G:TiO_2/WO_3 and H_2-Pt-G:TiO_2/WO_3 RPCs are displayed in **Figure 5a**. It can be observed that the typical absorption band of TiO_2 has been slightly shifted in the case of G:TiO_2/WO_3, whereas, it has been drastically shifted towards visible light region in the case of H_2-Pt-G:TiO_2/WO_3. In addition, a shoulder band is also observed around 490 nm, which could be attributed to the H_2 treatment and Pt deposition induced optical enhancement in H_2-Pt-G:TiO_2/WO_3 system [60,61]. These observed changes in the optical absorption profile of H_2-Pt-G:TiO_2/WO_3 could be attributed to the several factors such as the composite induced electron transitions in the system, oxygen vacancies induced optical enhancements and the synergistic optical enhancements due to the integration of multiple systems such as TiO_2, WO_3 and Pt along with the effect of carbon-based template and H_2 treatments. Furthermore, the band gap energy of these systems was calculated using Tauc plot [64], where the band gap energy of TiO_2, G:TiO_2/WO_3 and H_2-Pt-G:TiO_2/WO_3 was estimated to be 3.18,2.84 and 2.61 eV, respectively. The observed band gap reduction in G:TiO_2/WO_3 could be attributed to the composite formation-induced optical transition in the system, while a drastic reduction in the band gap energy of H_2-Pt-G:TiO_2/WO_3 was attributed to the synergistic effects in the optical transition between the TiO_2/WO_3/Pt systems along with the glucose template and H_2 treatment induced defective structures in the system.

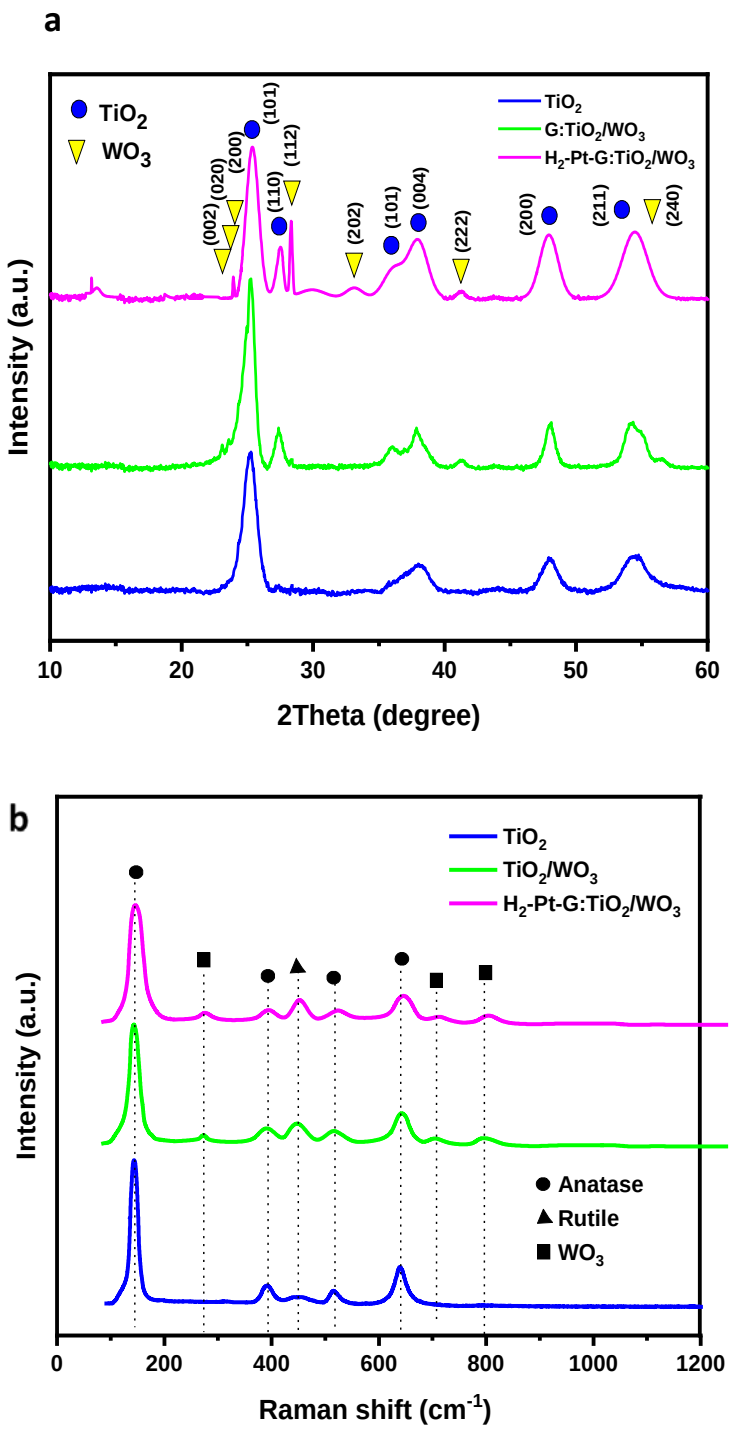

Figure 4. a) XRD and b) Raman spectra of the TiO_2, G:TiO_2/WO_3, and H_2-Pt-G:TiO_2/WO_3 samples.

Photoluminescence (PL) spectra were obtained to investigate the radiative recombination probabilities in the synthesized TiO_2, $G:TiO_2/WO_3$ and H_2-Pt-$G:TiO_2/WO_3$ photocatalyst systems (**Figure 5b**). As seen, the photoluminescence intensity of the H_2-Pt-$G:TiO_2/WO_3$ RPC has been significantly reduced as compared to other samples, which could be related to the lower e^-/h^+ recombination probability in H_2-Pt-$G:TiO_2/WO_3$. The radiative recombination is significantly reduced due to the heterojunction formation between TiO_2 and WO_3, where the photogenerated electrons and holes have been effectively separated at interface and drastically reduced their decay and recombination time. Furthermore, such recombination of charge carriers is further reduced in H_2-Pt-$G:TiO_2/WO_3$ due to the oxygen vacancies that effectively trap the electrons and slow down their recombination. Furthermore, the photographic image given as the insert in **Figure 5a**, the color of the sample is turned from white ($G:TiO_2/WO_3$) to grayish (H_2-Pt-$G:TiO_2/WO_3$) indicating that H_2-Pt-$G:TiO_2/WO_3$ can strongly absorb visible light photons, where such properties essentially originated due to the synergistic optical enhancements and existence oxygen vacancies in the system.

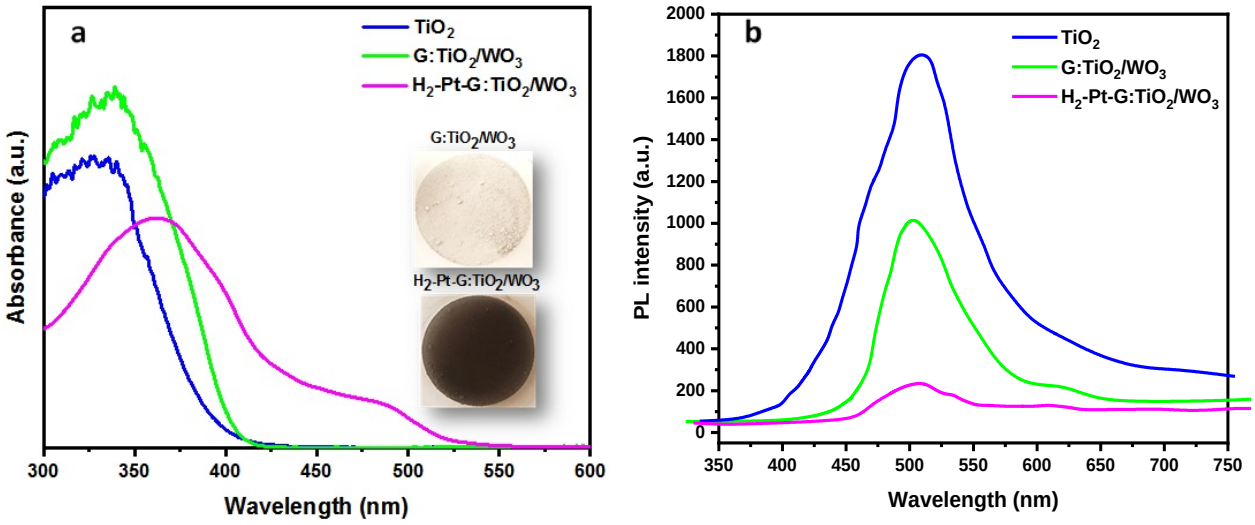

Figure 5. a) UV-vis and b) Photoluminescence (PL) spectra of the TiO_2, $G:TiO_2/WO_3$, and H_2-Pt-$G:TiO_2/WO_3$ samples.

The surface chemical states of Ti and W in $G:TiO_2/WO_3$ and H_2-Pt-$G:TiO_2/WO_3$ are studied by the X-ray photoelectron spectroscopy (XPS)technique (Figure 6 a-c). The normalized

Ti 2p XPS spectrum of G:TiO_2/WO_3 and H_2-Pt-G:TiO_2/WO_3 shows two peaks at 458.4 eV and 464.1 eV, which are characteristic of related to Ti^{4+} in TiO_2. A slight asymmetry of the Ti peak could be ascribed to the presence of Ti-C bonds at 460.2 eV and 466.2 eV possibly coming from the reaction with the glucose template [65,66]. The Ti 2p peak is known to display important changes depending on the chemical surrounding of the Ti atom and therefore by considering the similarities between the obtained Ti 2p, any changes in the bonding environment states due to the H_2 treatment can be excluded [67,68]. For G:TiO_2/WO_3 sample, only two XPS peaks at 38.4 and 36.3 eV which are characteristic of W^{6+} A change of shape for the W 4f peak is unambiguously observed in H_2-Pt-G:TiO_2/WO_3 RPC as compared to G:TiO_2/WO_3. By deconvoluting the peaks, a broadening of the W $4f_{7/2}$ and W $4f_{5/2}$ peaks is found in as a consequence of the H_2 treatment. The FWHM of both W $4f_{7/2}$ and W $4f_5$ peaks changes from 1.15±0.02 eV (G:TiO_2/WO_3) to 1.36±0.03 eV (H_2-Pt-G:TiO_2/WO_3). Peak broadening is typically associated to the chemical disorders in the system, which can be related to the formation of suboxide phases such as $WO_{3-\delta}$ in the reducing environment. An additional shoulder peak at lower binding does not present in the first case may also indicate a small amount (below ~3%) of W in the 4+ oxidation state. Therefore, a higher concentration for oxygen vacancies in the WO_{3-x} matrix can be attained due to H_2 treatment acting as trapping sites to store electrons. Moreover, the presence of these vacancies is displayed by the enhanced absorption in the visible light region, confirming that solar harvesting is remarkably improved [69,70].

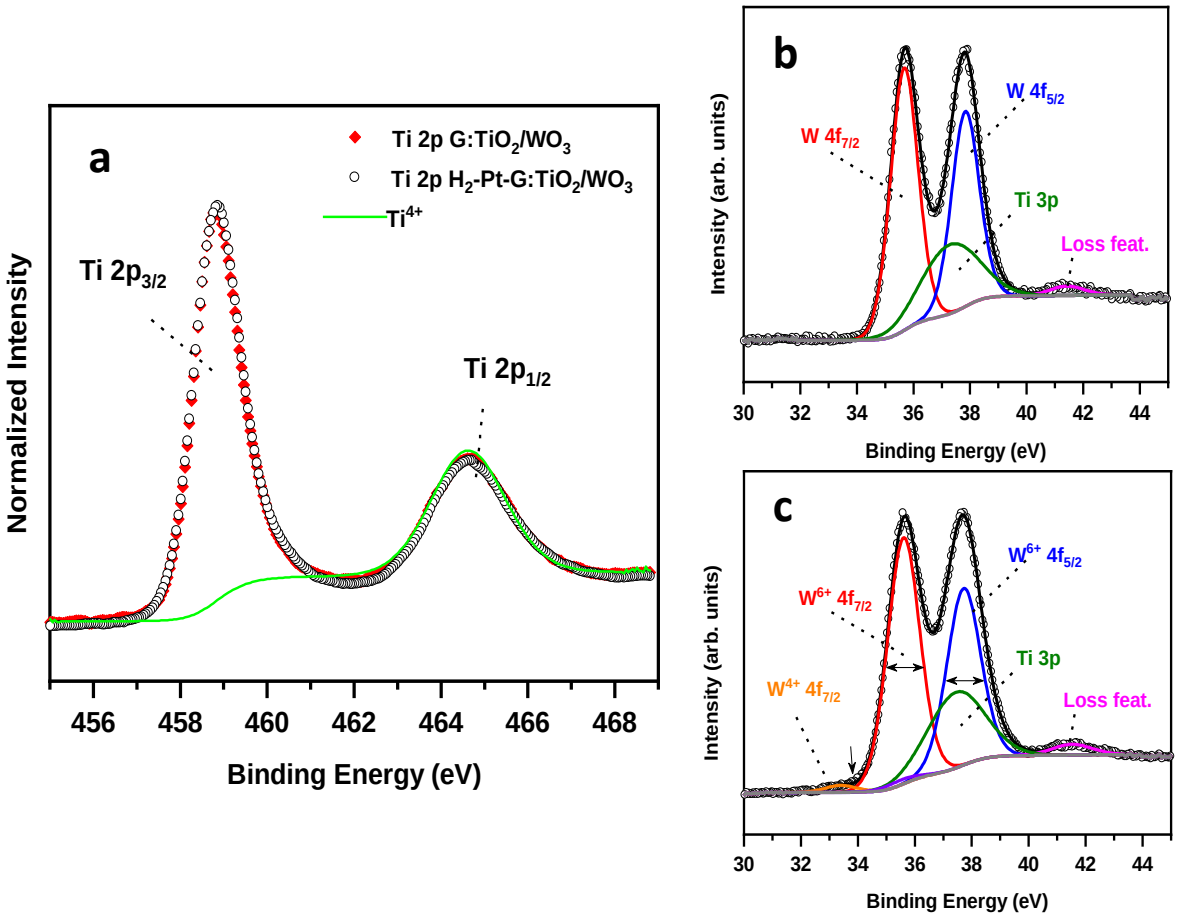

Figure 6. a-c) XPS narrow scan spectra(Ti 2p and W 4f) of G:TiO_2/WO_3, and H_2-Pt-G:TiO_2/WO_3 RPCs.

The surface properties of the different samples were studied using N_2 physical adsorption at 77 K. The specific surface area (S_{BET}) of H_2-Pt-G:TiO_2/WO_3 RPC was found to be 188 $m^2\ g^{-1}$, which is much higher than that of the TiO_2 (55 m^2g^{-1}), and G:TiO_2/WO_3 (112 m^2g^{-1}) (**Table 2**). This improved surface area of H_2-Pt-G:TiO_2/WO_3 RPC could be due to the synergistic effect of glucose-derived porous characteristics and H_2 treatment. It can be realized that the addition of D-glucose as the non-surfactant template fundamentally modifies the microstructure of the matrix leading to mesoporosity in the material. These pores or channel structures in the materials are formed upon the removal of glucose molecules by the calcination process [71]. Moreover, it is reported that S_{BET} is strongly dependent on H_2 treatment providing many active sites on the surface [72,73]. It is mostly observed that the increased these active sites and broadening in the range of mesopores lead to extend the adsorption towards the visible light, contributing a better photoactivity [74–76].

The photoactivity of the synthesized TiO_2, G:TiO_2/WO_3 and H_2-Pt-G:TiO_2/WO_3 RPC was investigated for their efficiency in MeOH decomposition under visible light ($\lambda \geq 420$ nm) and in dark conditions **(Figure 7)**. As seen, there was a significant enhancement in H_2-Pt-G:TiO_2/WO_3 was observed towards the decomposition of MeOH under both visible light and in dark conditions. The results showed that the G:TiO_2/WO_3 degraded around 33.15% of MeOH at the end of 2 h under light irradiation and up to 24 % in dark, whereas H_2-Pt-G:TiO_2/WO_3 degraded around 61% and 33% of MeOH in light and dark conditions, respectively. The observed increased decomposition rate under illumination over H_2-Pt-G:TiO_2/WO_3 could be attributed to their enhanced catalytic properties originated due to the presence of oxygen vacancies and Pt nanoparticles. Notably, Pt nanoparticles enable an efficient charge separation in the system as they provide pathways for the effective separation of the excited electrons [30,11]. Interestingly, after the light was turned off, the activity of H_2-Pt-G:TiO_2/WO_3 RPC was still progressed with higher rate than G:TiO_2/WO_3. The reason for such activity under dark conditions may be attributed to the H_2 treatment-induced creation of defects in TiO_2/WO_3 heterostructure that probably introduced/improved the electron storage ability in the system. During the light irradiation, a portion of electrons involved in the photocatalytic reactions, while the remaining electrons were stored in the defective structures of TiO_2/WO_3 heterostructure and once the light was turned off, these stored electrons get released and continued the catalytic reactions. Especially, the activity of H_2-Pt-G:TiO_2/WO_3 under dark conditions could be attributed to the electron storage ability of the defective WO_3 system, which supplied the stored electrons under dark to react with the surrounding molecules to degrade MeOH. In this process, the domains of WO_{3-x} on the TiO_{2-y} surface acted as the acceptor of photo-promoted CB electrons, which in turn increased the efficiency of charge carrier separation, since W^{6+} ions could be easily reduced to W^{5+}. Notably, the developed synthetic route seems to be efficient to couple the two oxides and metal NPs, which eventually led to the effective formation of a system with improved electron storage abilities [77,78]. To have a comparison on photoactivity performance, some of the recent researches working on TiO_2/ WO_3 based structures are listed in **Table 3**.

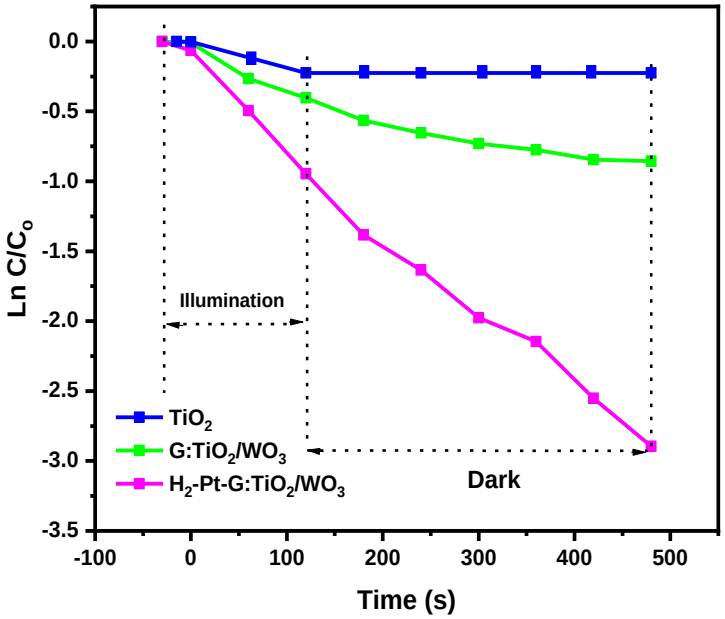

Figure 7. Decomposition of MeOH as a function of reaction time under visible light illumination and in the dark for the samples.

Table 2: Anatase phase ration, kinetic constants of photocatalytic MeOH decomposition under solar light and in the dark, and BET surface area (m^2/g) for the TiO_2, G:TiO_2/WO_3, and H_2-Pt-G:TiO_2/WO_3

Sample name	Anatase phase wt%	K (min^{-1}) Illumination	R^2	K (min^{-1}) Dark	R^2	Surface area ($m^2 \cdot g^{-1}$)
TiO_2	93	n/a	0.939	n/a	0.9923	77.9
G:TiO_2/WO_3	80	-0.00329	0.96961	-0.00122	0.93872	112.2
H_2-Pt-G:TiO_2/WO_3	71	-0.00736	0.99015	-0.00524	0.99071	188

To understand the observed enhanced efficiencies in H_2-Pt-G:TiO_2/WO_3 RPC, study of the space charge at the TiO_2/WO_3 interface is important. Therefore, the Mott-Schottky (M-S) measurement was realized to be a potential technique to reveal both the dopant density and flat band potential at semiconductor/liquid contacts [79,80]. **Figure 8a** shows the Mott–Schottky (C^{-2}A–V) plots for the synthesized systems, indicating a positive slope for all four samples meaning that they are n-type semiconductors. As can be seen in **Figure 8a**, the flat-band potential (V_{fb}) can be measured b -0.68, -0.84, and -1 V (versus SCE)for the TiO_2, G:TiO_2/WO_3 and H_2-Pt-G:TiO_2/WO_3, respectively. Compared with other samples, the V_{fb} of H_2-Pt-G:TiO_2/WO_3 has been found to have

a lower potential, confirming attributing to a higher carrier concentration and charge transfer possibly due to the existence of oxygen vacancies created by H_2 thermal treatment. Accordingly, H_2-Pt-G:TiO_2/WO_3 exhibited the highest photoactivity. The Mott–Schottky equation can be given through the following equation:

$$\frac{dC^{-2}}{dV} = -\frac{2}{\varepsilon\varepsilon_o A^2 e N_D}\left(V - V_{fb} - \frac{k_B T}{e}\right)$$

Where, e is the electronic charge ($1.60*10^{19}$ C), ε_o is the vacuum permittivity ($8.85*10^{12}$ Fm^{-1}), ε the relative dielectricconstant (10^5 was estimated for TiO_2/WO_3 system) [81], C and Aare the interfacial capacitance and area, respectively, N_D the number of donors, V the applied voltage, k_B is Boltzmann's constant and T is the absolute temperature. The value of N_D can also be determined from the slope of a plot of $1/C^2$ (on Y-axis) versus V (X-axis), knowing ε conveniently.

Table 3. Photocatalytic degradation of different pollutants over TiO_2/ WO_3 based photocatalysts.

Composite	Light source	Degradation time under illumination/Rate	Dye Concentration	Dye type	Photocatalyst amount
Pt-WO_3/TiO_2 [38]	visible light	24 h / 60.6 %	17.2 µmol	Acetic acid	50 mg
TiO_2/WO_3 [82]	visible light	120 min/ 31 %	1 ppm	Acetaldehyde	0.1 gL^{-1}
carbon-doped crystalline TiO_2 [83]	visible light	300 min/ 60 %	100 mL, 5 mg/L	RhB	10 mg
TiO_2/WO_3 [84]	simulated sunlight	12 h/ 60 %	8 mg/L	dihydroxybenzoic acid	Thin film
TiO_2/WO_3 [84]	Vis light	8 h/ 80 %	30 mg/L, 500 mL	Acid red	0.2 g/L
N-doped TiO_2/WO_3 [85]	visible light	180 min/ 40 %	1.2 ppm	hexane	0.5 g
TiO_2/WO_3 [86]	UV light	120 min/ 80 %	2 × 10−4 M	4- chlorophenol	1.2 g/L
TiO_2/WO_3/GO [87]	sunlight	7 h/ 90 %	50 ml, 10 mg/l	bisphenol A	2 mg
TiO_2/WO_3 [88]	UV light	210 min/ 57 %	2 × 10−5 mol L^{-1}	Methylene blue	0.1 g L−1
TiO_2/WO_3 [89]	visible light	300 min/ 15 %	10−3 M	4-chlorophenol	Thin film

The donor density is found to be increased in the following order, $3.9*10^{17}$, $1.1*10^{18}$, and $1.55*10^{18}$ cm^{-3} for TiO_2, G:TiO_2/WO_3 and H_2-Pt-G:TiO_2/WO_3, respectively. Furthermore, H_2-Pt-G:TiO_2/WO_3 RPC has a higher donor density than that of TiO_2 and G:TiO_2/WO_3 systems indicating an increase in the charge separation performance. The increased donor density enhances both the charge transport in the samples due to the H_2 treatment and the electron transfer in interface of the material and FTO substrate. Furthermore, the increased electron density in the H_2 treated system i.e. H_2-Pt-G:TiO_2/WO_3 could led to shift of TiO_2 Fermi level towards the CB, facilitating the enhanced charge separation at the H_2-Pt-G:TiO_2/WO_3/electrolyte interface [90].

As to further validate the observations, the photocurrent density measurements (**Figure 8b**) were performed under irradiation to evaluate the separation of the electron/hole pairs in the synthesized materials. It is observed that H_2-Pt-G:TiO_2/WO_3 RPC shows higher photocurrent density as compared to other samples (about 100 $\mu A/cm^2$). Such enhancement in H_2-Pt-G:TiO_2/WO_3 can be related to appropriate interfacial contacts between TiO_2-WO_3, rutile fractions in TiO_2 and the enhanced oxygen vacancies.

In accordance with the photocurrent density properties, the observed smaller semicircle in the Nyquist plot (**Figure 8c**) of H_2-Pt-G:TiO_2/WO_3 RPC demonstrates the existence of lower charge transfer resistance and efficient transport and separation of electron-hole pairs in the system [91,92]. Notably, the Nyquist plots indicated that the TiO_2 had a very large arc radius, which essentially represented the higher charge transfer [93,94]. It can be seen that the arc radius of H_2-Pt-G:TiO_2/WO_3 RPC is smaller than that of TiO_2 and G:TiO_2/WO_3. This smallest radius of the arc essentially indicates the minimal resistance i.e. the maximum charge separation and transfer process in the system.

These results may indicate superior photocatalytic activity of H_2-Pt-G:TiO_2/WO_3 RPC, implying that the oxygen vacancies and Pt cocatalyst have played a key role in enhancing the charge separations and transportations. As the electrons were effectively transferred to different sites due to presence of Pt nanoparticles, more number of holes participated in the decomposition of methanol and increased the photocatalytic activity of H_2-Pt-G:TiO_2/WO_3 RPC. Moreover, large amounts of oxygen vacancies are formed due to the H_2 treatment, which led to the formation of defective band structures in the band gaps of the host system. Furthermore, as a matter of fact, there were more trapping sites available for the storage of electrons essentially due to an upshift

in the Fermi level caused by the defect bands. Therefore, these oxygen vacancies were desirable for the separation of the photogenerated electron–hole pairs [13]. In addition to this, a multi-electron reduction of O_2 over Pt was also facilitated, which eventually supported towards the enhanced MeOH decomposition under visible light and dark conditions.

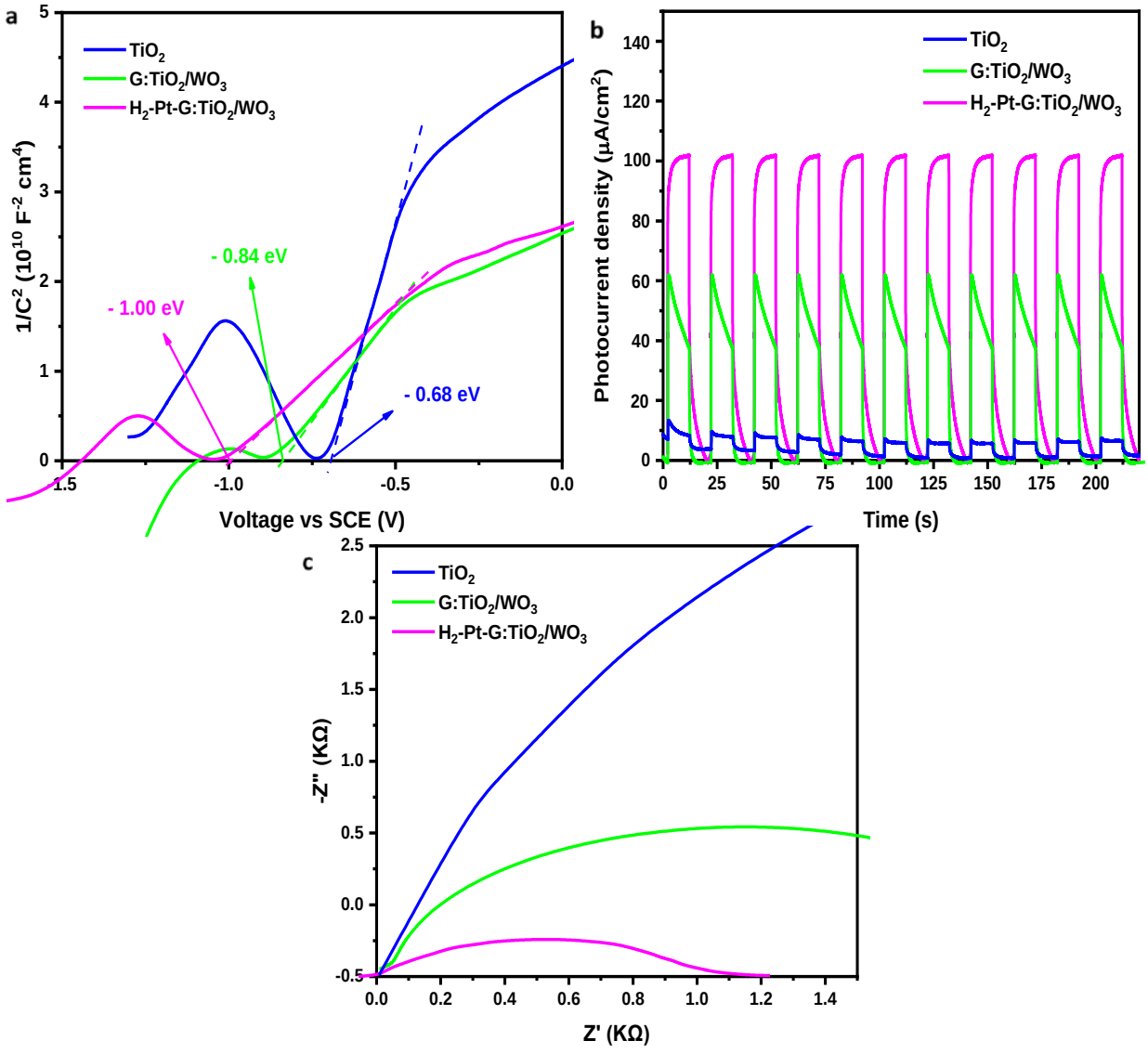

Figure 8. a) Mott-Schottky plots and calculated flat band potentials, b) photocurrent response, and c) electrochemical impedance spectroscopy (EIS) Nyquist plots of the for TiO_2, $G:TiO_2/WO_3$, and H_2-Pt-$G:TiO_2/WO_3$.

4. Conclusion

In this paper, we reported a new PRC named the H_2-Pt-G:TiO_2/WO_3 RPC and studied its structure and performance to photodegrade of pollutants round the clock. By comparing the morphology of the samples, the H_2-Pt-G:TiO_2/WO_3 agglomeration was found to be increased attributing to its relatively reduced particle size affected by H_2 treatment and Pt deposition. The XRD results showed increasing in rutile content for this sample affected by the thermal template removal, formation of crystalline WO_3 and H_2 treatment process. The Raman profiles confirmed decreasing of crystallite size and defects-mediated structural changes in the H_2-Pt-G:TiO_2/WO_3. A shift in UV absorption towards visible light and a shoulder band around 490 nm in the case of the H_2-Pt-G:TiO_2/WO_3 were observed attributing to the oxygen vacancies and the optical enhancements due to effect of our multiple system including TiO_2, WO_3 and Pt. Furthermore, decreasing the band gap energy of this sample could be attributed to the optical transition in the TiO_2/WO_3/Pt system and defective structures due to the glucose template and H_2 treatment. A high oxygen vacancy concentration in the WO_{3-x} matrix confirmed by XPS achieving after H_2 treatment which is demonstrated by the enhanced absorption in the visible light. Moreover, lower charge recombination rate and higher surface area affected by H_2 treatment for the H_2-Pt-G:TiO_2/WO_3 RPC were confirmed by PL and BET analyses respectively. The photoactivity results presented that the H_2-Pt-G:TiO_2/WO_3 degraded MeOH around 61% and 33% in light and dark, respectively. The improvement could be related to higher surface area, the presence of oxygen vacancies, effect of Pt nanoparticles and the electron storage ability of the defective WO_3 system. Electrochemical measurements confirmed a better performance in the H_2-Pt-G:TiO_2/WO_3 relating to an appropriate interfacial contacts TiO_2/WO_3 and a maximum charge separation/ transfer in the system due to existence of oxygen vacancies.

Acknowledgments

This work was partially funded by the Natural Sciences and Engineering Research Council of Canada (NSERC) through the Strategic Project (PS) and Discovery Grants. This work was also supported by MIUR, PRIN 2015WBEP3H “Monitoraggio, Consolidamento, Conservazione e Protezione di Beni Culturali”.

References

(1) Yang, S.; Tang, W.; Ishikawa, Y.; Feng, Q. Synthesis of Titanium Dioxide with Oxygen Vacancy and Its Visible-Light Sensitive Photocatalytic Activity. *Mater. Res. Bull.* **2011**. https://doi.org/10.1016/j.materresbull.2011.01.004.

(2) Su, J.; Yu, S.; Xu, M.; Guo, Y.; Sun, X.; Fan, Y.; Zhang, Z.; Yan, J.; Zhao, W. Enhanced Visible Light Photocatalytic Performances of Few-Layer MoS2@TiO2 Hollow Spheres Heterostructures. *Mater. Res. Bull.* **2020**. https://doi.org/10.1016/j.materresbull.2020.110936.

(3) Liu, W.; Du, T.; Ru, Q.; Zuo, S.; Cai, Y.; Yao, C. Preparation of Graphene/WO3/TiO2 Composite and Its Photocathodic Protection Performance for 304 Stainless Steel. *Mater. Res. Bull.* **2018**. https://doi.org/10.1016/j.materresbull.2018.03.012.

(4) Takahashi, Y.; Tatsuma, T. Oxidative Energy Storage Ability of a TiO2-Ni(OH)2 Bilayer Photocatalyst. *Langmuir* **2005**. https://doi.org/10.1021/la052107b.

(5) Huang, H.; Jiang, L.; Zhang, W. K.; Gan, Y. P.; Tao, X. Y.; Chen, H. F. Photoelectrochromic Properties and Energy Storage of TiO2-XNx/NiO Bilayer Thin Films. *Sol. Energy Mater. Sol. Cells* **2010**. https://doi.org/10.1016/j.solmat.2009.10.013.

(6) Buama, S.; Junsukhon, A.; Ngaotrakanwiwat, P.; Rangsunvigit, P. Validation of Energy Storage of TiO2[Sbnd]NiO/TiO2 Film by Electrochemical Process and Photocatalytic Activity. *Chem. Eng. J.* **2017**. https://doi.org/10.1016/j.cej.2016.10.093.

(7) Tatsuma, T.; Saitoh, S.; Ngaotrakanwiwat, P.; Ohko, Y.; Fujishima, A. Energy Storage of TiO2-WO3 Photocatalysis Systems in the Gas Phase. *Langmuir* **2002**, *18* (21), 7777–7779. https://doi.org/10.1021/la026011i.

(8) Kim, S.; Park, H. Sunlight-Harnessing and Storing Heterojunction TiO2/Al 2O3/WO3 Electrodes for Night-Time Applications. *RSC Adv.* **2013**, *3* (38), 17551–17558. https://doi.org/10.1039/c3ra42644k.

(9) Takahashi, Y.; Tatsuma, T. Visible Light-Induced Photocatalysts with Reductive Energy

Storage Abilities. *Electrochem. commun.* **2008**, *10* (9), 1404–1407. https://doi.org/10.1016/j.elecom.2008.07.026.

(10) Dohcevic-Mitrovic, Z.; Stojadinović, S.; Lozzi, L.; Aškrabić, S.; Rosić, M.; Tomić, N.; Paunović, N.; Lazović, S.; Nikolić, M. G.; Santucci, S. WO3/TiO2 Composite Coatings: Structural, Optical and Photocatalytic Properties. *Mater. Res. Bull.* **2016**. https://doi.org/10.1016/j.materresbull.2016.06.011.

(11) Nguyen, C. C.; Vu, N. N.; Do, T. O. Efficient Hollow Double-Shell Photocatalysts for the Degradation of Organic Pollutants under Visible Light and in Darkness. *J. Mater. Chem. A* **2016**. https://doi.org/10.1039/c5ta09016d.

(12) Wei, Y.; Huang, Y.; Fang, Y.; Zhao, Y.; Luo, D.; Guo, Q.; Fan, L.; Wu, J. Hollow Mesoporous TiO2/WO3 Sphere Heterojunction with High Visible-Light-Driven Photocatalytic Activity. *Mater. Res. Bull.* **2019**. https://doi.org/10.1016/j.materresbull.2019.110571.

(13) Liu, Q.; Wang, F.; Lin, H.; Xie, Y.; Tong, N.; Lin, J.; Zhang, X.; Zhang, Z.; Wang, X. Surface Oxygen Vacancy and Defect Engineering of WO3 for Improved Visible Light Photocatalytic Performance. *Catal. Sci. Technol.* **2018**. https://doi.org/10.1039/c8cy00994e.

(14) Pan, X.; Yang, M. Q.; Fu, X.; Zhang, N.; Xu, Y. J. Defective TiO2 with Oxygen Vacancies: Synthesis, Properties and Photocatalytic Applications. *Nanoscale*. 2013. https://doi.org/10.1039/c3nr00476g.

(15) Zhang, L.; Wang, S.; Lu, C. Detection of Oxygen Vacancies in Oxides by Defect-Dependent Cataluminescence. *Anal. Chem.* **2015**. https://doi.org/10.1021/acs.analchem.5b02267.

(16) Tian, J.; Zhao, Z.; Kumar, A.; Boughton, R. I.; Liu, H. Recent Progress in Design, Synthesis, and Applications of One-Dimensional TiO2 Nanostructured Surface Heterostructures: A Review. *Chemical Society Reviews*. 2014. https://doi.org/10.1039/c4cs00180j.

(17) Kim, H. S.; Kang, S. H. Effect of Hydrogen Treatment on Anatase TiO2 Nanotube Arrays for Photoelectrochemical Water Splitting. *Bull. Korean Chem. Soc.* **2013**. https://doi.org/10.5012/bkcs.2013.34.7.2067.

(18) Liu, Y.; Liu, C.; Li, J. Flexible Free-Standing Hydrogen-Treated Titanium Dioxide Nanowire Arrays as a High Performance Anode for Lithium Ion Batteries. *J. Mater. Chem. A* **2014**. https://doi.org/10.1039/c4ta03495c.

(19) Wang, G.; Ling, Y.; Wang, H.; Yang, X.; Wang, C.; Zhang, J. Z.; Li, Y. Hydrogen-Treated WO 3 Nanoflakes Show Enhanced Photostability. *Energy Environ. Sci.* **2012**. https://doi.org/10.1039/c2ee03158b.

(20) Wheeler, D. A.; Ling, Y.; Dillon, R. J.; Fitzmorris, R. C.; Dudzik, C. G.; Zavodivker, L.; Rajh, T.; Dimitrijevic, N. M.; Millhauser, G.; Bardeen, C.; Li, Y.; Zhang, J. Z. Probing the Nature of Bandgap States in Hydrogen-Treated TiO2 Nanowires. *J. Phys. Chem. C* **2013**. https://doi.org/10.1021/jp409857j.

(21) Al Mohammad, A.; Gillet, M. Phase Transformations in WO3 Thin Films during Annealing. *Thin Solid Films* **2002**. https://doi.org/10.1016/S0040-6090(02)00090-1.

(22) Ramana, C. V.; Utsunomiya, S.; Ewing, R. C.; Julien, C. M.; Becker, U. Structural Stability and Phase Transitions in WO3 Thin Films. *J. Phys. Chem. B* **2006**, *110* (21), 10430–10435. https://doi.org/10.1021/jp056664i.

(23) LeGore, L. J.; Lad, R. J.; Moulzolf, S. C.; Vetelino, J. F.; Frederick, B. G.; Kenik, E. A. Defects and Morphology of Tungsten Trioxide Thin Films. *Thin Solid Films* **2002**. https://doi.org/10.1016/S0040-6090(02)00047-0.

(24) Li, M.; Altman, E. I.; Posadas, A.; Ahn, C. H. Surface Phase Transitions and Related Surface Defect Structures upon Reduction of Epitaxial WO3(100) Thin Films: A Scanning Tunneling Microscopy Study. *J. Vac. Sci. Technol. A Vacuum, Surfaces, Film.* **2004**. https://doi.org/10.1116/1.1756880.

(25) Joo, J. B.; Zhang, Q.; Lee, I.; Dahl, M.; Zaera, F.; Yin, Y. Mesoporous Anatase Titania Hollow Nanostructures Though Silica-Protected Calcination. *Adv. Funct. Mater.* **2012**, *22* (1), 166–174. https://doi.org/10.1002/adfm.201101927.

(26) Jiang, P.; Bertone, J. F.; Colvin, V. L. A Lost-Wax Approach to Monodisperse Colloids and Their Crystals. *Science (80-.).* **2001**, *291* (5503), 453–457. https://doi.org/10.1126/science.291.5503.453.

(27) Lou, X. W.; Archer, L. A. A General Route to Nonspherical Anatase TiO2 Hollow Colloids and Magnetic Multifunctional Particles. *Adv. Mater.* **2008**, *20* (10), 1853–1858. https://doi.org/10.1002/adma.200702379.

(28) Zhou, H.; Kang, M.; Qin, B.; Zhao, N.; Wu, D.; Lv, B.; Wang, Q. Glucose-Mediated Template-Free Synthesis of Hollow CuO Microspheres. *RSC Adv.* **2018**, *8* (26), 14157–14163. https://doi.org/10.1039/c8ra00684a.

(29) Kartini, I.; Evana; Chotimah. Glucose Templated Hydrothermal Synthesis of Porous Nanocrystalline Anatase TiO2. *Asian J. Chem.* **2010**.

(30) Nguyen, C. C.; Nguyen, D. T.; Do, T. O. A Novel Route to Synthesize C/Pt/TiO2 Phase Tunable Anatase–Rutile TiO2 for Efficient Sunlight-Driven Photocatalytic Applications. *Appl. Catal. B Environ.* **2018**. https://doi.org/10.1016/j.apcatb.2017.12.038.

(31) Nguyen, D. T.; Nguyen, C. C.; St-Jean, M.; Chabot, S.; Kaliaguine, S.; Do, T. O. All in One: Contributions of Ni Dopants and Ni/NiS Dual Cocatalysts to the Enhanced Efficiency of TiO2 Photocatalyst for the Degradation of Organic Pollutants. *ACS Appl. Nano Mater.* **2018**. https://doi.org/10.1021/acsanm.8b01693.

(32) Semlali, S.; Pigot, T.; Flahaut, D.; Allouche, J.; Lacombe, S.; Nicole, L. Mesoporous Pt-TiO2 Thin Films: Photocatalytic Efficiency under UV and Visible Light. *Appl. Catal. B Environ.* **2014**. https://doi.org/10.1016/j.apcatb.2013.12.042.

(33) Denny, F.; Scott, J.; Chiang, K.; Teoh, W. Y.; Amal, R. Insight towards the Role of Platinum in the Photocatalytic Mineralisation of Organic Compounds. *J. Mol. Catal. A Chem.* **2007**. https://doi.org/10.1016/j.molcata.2006.08.031.

(34) He, C.; Xiong, Y.; Zhu, X.; Li, X. A Platinised TiO2 Film with Both Photocatalytic and Non-Photocatalytic Activities towards the Oxidation of Formic Acid. *Appl. Catal. A Gen.* **2004**. https://doi.org/10.1016/j.apcata.2004.07.020.

(35) Hwang, S.; Lee, M. C.; Choi, W. Highly Enhanced Photocatalytic Oxidation of CO on Titania Deposited with Pt Nanoparticles: Kinetics and Mechanism. *Appl. Catal. B Environ.* **2003**. https://doi.org/10.1016/S0926-3373(03)00162-0.

(36) Markoví, N. M.; Ross, P. N. Surface Science Studies of Model Fuel Cell Electrocatalysts.

Surf. Sci. Rep. **2002**. https://doi.org/10.1016/s0167-5729(01)00022-x.

(37) Hinde, C. S.; Ansovini, D.; Wells, P. P.; Collins, G.; Aswegen, S. Van; Holmes, J. D.; Hor, T. S. A.; Raja, R. Elucidating Structure-Property Relationships in the Design of Metal Nanoparticle Catalysts for the Activation of Molecular Oxygen. *ACS Catal.* **2015**. https://doi.org/10.1021/acscatal.5b00481.

(38) Higashimoto, S.; Katsuura, K.; Yamamoto, M.; Takahashi, M. Photocatalytic Activity for Decomposition of Volatile Organic Compound on Pt-WO3 Enhanced by Simple Physical Mixing with TiO2. *Catal. Commun.* **2020**. https://doi.org/10.1016/j.catcom.2019.105831.

(39) Li, X. Z.; Li, F. B.; Yang, C. L.; Ge, W. K. Photocatalytic Activity of WOx-TiO2 under Visible Light Irradiation. *J. Photochem. Photobiol. A Chem.* **2001**, *141* (2–3), 209–217. https://doi.org/10.1016/S1010-6030(01)00446-4.

(40) Khan, H.; Rigamonti, M. G.; Patience, G. S.; Boffito, D. C. Spray Dried TiO2/WO3 Heterostructure for Photocatalytic Applications with Residual Activity in the Dark. *Appl. Catal. B Environ.* **2018**. https://doi.org/10.1016/j.apcatb.2017.12.049.

(41) Park, J.; Lim, J.; Park, Y.; Han, D. S.; Shon, H. K.; Hoffmann, M. R.; Park, H. In Situ-Generated Reactive Oxygen Species in Precharged Titania and Tungsten Trioxide Composite Catalyst Membrane Filters: Application to As(III) Oxidation in the Absence of Irradiation. *Environ. Sci. Technol.* **2020**. https://doi.org/10.1021/acs.est.0c01550.

(42) Spurr, R. A.; Myers, H. Quantitative Analysis of Anatase-Rutile Mixtures with an X-Ray Diffractometer. *Anal. Chem.* **1957**, *29* (5), 760–762. https://doi.org/10.1021/ac60125a006.

(43) Meng, A.; Zhang, J.; Xu, D.; Cheng, B.; Yu, J. Enhanced Photocatalytic H2-Production Activity of Anatase TiO2 Nanosheet by Selectively Depositing Dual-Cocatalysts on (101) and (001) Facets. *Appl. Catal. B Environ.* **2016**, *198*, 286–294. https://doi.org/10.1016/j.apcatb.2016.05.074.

(44) Gao, X.; Wachs, I. E. Titania-Silica as Catalysts: Molecular Structural Characteristics and Physico-Chemical Properties. *Catal. Today* **1999**, *51* (2), 233–254. https://doi.org/10.1016/S0920-5861(99)00048-6.

(45) Bagherzadeh, M.; Kaveh, R.; Ozkar, S.; Akbayrak, S. Preparation and Characterization of

a New CdS–NiFe2O4/Reduced Graphene Oxide Photocatalyst and Its Use for Degradation of Methylene Blue under Visible Light Irradiation. *Res. Chem. Intermed.* **2018**, *44* (10), 5953–5979. https://doi.org/10.1007/s11164-018-3466-1.

(46) Adhikari, S.; Sarkar, D. High Efficient Electrochromic WO3 Nanofibers. *Electrochim. Acta* **2014**, *138*, 115–123. https://doi.org/10.1016/j.electacta.2014.06.062.

(47) Murcia, J. J.; Hidalgo, M. C.; Navío, J. A.; Vaiano, V.; Ciambelli, P.; Sannino, D. Photocatalytic Ethanol Oxidative Dehydrogenation over Pt/TiO 2: Effect of the Addition of Blue Phosphors. *Int. J. Photoenergy* **2012**. https://doi.org/10.1155/2012/687262.

(48) Yang, H. G.; Sun, C. H.; Qiao, S. Z.; Zou, J.; Liu, G.; Smith, S. C.; Cheng, H. M.; Lu, G. Q. Anatase TiO2 Single Crystals with a Large Percentage of Reactive Facets. *Nature* **2008**. https://doi.org/10.1038/nature06964.

(49) Beyer, J.; Mamakhel, A.; Søndergaard-Pedersen, F.; Yu, J.; Iversen, B. B. Continuous Flow Hydrothermal Synthesis of Phase Pure Rutile TiO2 Nanoparticles with a Rod-like Morphology. *Nanoscale* **2020**. https://doi.org/10.1039/c9nr09069j.

(50) Zhang, Q.; Gao, L.; Guo, J. Effects of Calcination on the Photocatalytic Properties of Nanosized TiO2 Powders Prepared by TiCl4 Hydrolysis. *Appl. Catal. B Environ.* **2000**, *26* (3), 207–215. https://doi.org/10.1016/S0926-3373(00)00122-3.

(51) Li, Y.; Fan, Y.; Chen, Y. A Novel Method for Preparation of Nanocrystalline Rutile TiO2 Powders by Liquid Hydrolysis of TiCl4. *J. Mater. Chem.* **2002**, *12* (5), 1387–1390. https://doi.org/10.1039/b200018k.

(52) Zhu, Z.; He, X.; Zhao, Y.; Ren, Q. Influence of WO3 Additive on Crystallite Structural Transformation of TiO2 Powders. *Xiyou Jinshu Cailiao Yu Gongcheng/Rare Met. Mater. Eng.* **2010**, *39* (5), 771–774. https://doi.org/10.1016/s1875-5372(10)60099-9.

(53) Couselo, N.; García Einschlag, F. S.; Candal, R. J.; Jobbágy, M. Tungsten-Doped TiO2 vs Pure TiO2 Photocatalysts: Effects on Photobleaching Kinetics and Mechanism. *J. Phys. Chem. C* **2008**, *112* (4), 1094–1100. https://doi.org/10.1021/jp0769781.

(54) Patra, S.; Andriamiadamanana, C.; Tulodziecki, M.; Davoisne, C.; Taberna, P. L.; Sauvage, F. Low-Temperature Electrodeposition Approach Leading to Robust Mesoscopic Anatase

TiO2 Films. *Sci. Rep.* **2016**, *6*. https://doi.org/10.1038/srep21588.

(55) Djerad, S.; Tifouti, L.; Crocoll, M.; Weisweiler, W. Effect of Vanadia and Tungsten Loadings on the Physical and Chemical Characteristics of V2O5-WO3/TiO2 Catalysts. *J. Mol. Catal. A Chem.* **2004**, *208* (1–2), 257–265. https://doi.org/10.1016/j.molcata.2003.07.016.

(56) Ren, G.; Gao, Y.; Yin, J.; Xing, A.; Liu, H. Synthesis of High-Activity TiO2/WO3 Photocatalyst via Environmentally Friendly and Microwave Assisted Hydrothermal Process. *J. Chem. Soc. Pakistan* **2011**, *33* (5), 666–670.

(57) Ponnusamy, R.; Gangan, A.; Chakraborty, B.; Sekhar Rout, C. Tuning the Pure Monoclinic Phase of WO3 and WO3-Ag Nanostructures for Non-Enzymatic Glucose Sensing Application with Theoretical Insight from Electronic Structure Simulations. *J. Appl. Phys.* **2018**. https://doi.org/10.1063/1.5010826.

(58) Woodward, P. M.; Sleight, A. W.; Vogt, T. Ferroelectric Tungsten Trioxide. *J. Solid State Chem.* **1997**. https://doi.org/10.1006/jssc.1997.7268.

(59) Thummavichai, K.; Wang, N.; Xu, F.; Rance, G.; Xia, Y.; Zhu, Y. In Situ Investigations of the Phase Change Behaviour of Tungsten Oxide Nanostructures. *R. Soc. Open Sci.* **2018**. https://doi.org/10.1098/rsos.171932.

(60) Vemuri, R. S.; Bharathi, K. K.; Gullapalli, S. K.; Ramana, C. V. Effect of Structure and Size on the Electrical Properties of Nanocrystalline WO3 Films. *ACS Appl. Mater. Interfaces* **2010**. https://doi.org/10.1021/am1004514.

(61) Govender, M.; Mwakikunga, B. W.; Machatine, A. G. J.; Kunert, H. W. Electrical and Optical Properties of Mixed Phase Tungsten Trioxide Films Grown by Laser Pyrolysis. *Phys. Status Solidi Curr. Top. Solid State Phys.* **2014**. https://doi.org/10.1002/pssc.201300212.

(62) Pokhrel, S.; Birkenstock, J.; Dianat, A.; Zimmermann, J.; Schowalter, M.; Rosenauer, A.; Ciacchi, L. C.; Mädler, L. In Situ High Temperature X-Ray Diffraction, Transmission Electron Microscopy and Theoretical Modeling for the Formation of WO3 Crystallites. *CrystEngComm* **2015**. https://doi.org/10.1039/c5ce00526d.

(63) Battu, A. K.; Manandhar, S.; Ramana, C. V. Molybdenum Incorporation Induced Enhancement in the Mechanical Properties of Gallium Oxide Films. *Adv. Mater. Interfaces* **2017**. https://doi.org/10.1002/admi.201700378.

(64) Sun, W.; Zhou, S.; You, B.; Wu, L. Facile Fabrication and High Photoelectric Properties of Hierarchically Ordered Porous TiO 2. *Chem. Mater.* **2012**, *24* (19), 3800–3810. https://doi.org/10.1021/cm302464g.

(65) Akhavan, O.; Ghaderi, E. Photocatalytic Reduction of Graphene Oxide Nanosheets on TiO2 Thin Film for Photoinactivation of Bacteria in Solar Light Irradiation. *J. Phys. Chem. C* **2009**. https://doi.org/10.1021/jp906325q.

(66) Akhavan, O.; Ghaderi, E.; Rahimi, K. Adverse Effects of Graphene Incorporated in TiO 2 Photocatalyst on Minuscule Animals under Solar Light Irradiation. *J. Mater. Chem.* **2012**. https://doi.org/10.1039/c2jm35228a.

(67) Nguyen-Phan, T. D.; Luo, S.; Liu, Z.; Gamalski, A. D.; Tao, J.; Xu, W.; Stach, E. A.; Polyansky, D. E.; Senanayake, S. D.; Fujita, E.; Rodriguez, J. A. Striving Toward Noble-Metal-Free Photocatalytic Water Splitting: The Hydrogenated-Graphene-TiO2 Prototype. *Chem. Mater.* **2015**. https://doi.org/10.1021/acs.chemmater.5b02131.

(68) Eom, J. Y.; Lim, S. J.; Lee, S. M.; Ryu, W. H.; Kwon, H. S. Black Titanium Oxide Nanoarray Electrodes for High Rate Li-Ion Microbatteries. *J. Mater. Chem. A* **2015**. https://doi.org/10.1039/c5ta01718a.

(69) Wu, R.; Zhang, J.; Shi, Y.; Liu, D.; Zhang, B. Metallic WO2-Carbon Mesoporous Nanowires as Highly Efficient Electrocatalysts for Hydrogen Evolution Reaction. *J. Am. Chem. Soc.* **2015**. https://doi.org/10.1021/jacs.5b01330.

(70) Yan, J.; Wang, T.; Wu, G.; Dai, W.; Guan, N.; Li, L.; Gong, J. Tungsten Oxide Single Crystal Nanosheets for Enhanced Multichannel Solar Light Harvesting. *Adv. Mater.* **2015**. https://doi.org/10.1002/adma.201404792.

(71) Wei, Y.; Xu, J.; Dong, H.; Dong, J. H.; Qiu, K.; Jansen-Varnum, S. A. Preparation and Physisorption Characterization of D-Glucose-Templated Mesoporous Silica Sol-Gel Materials. *Chem. Mater.* **1999**, *11* (8), 2023–2029. https://doi.org/10.1021/cm981004u.

(72) Serpone, N. Heterogeneous Photocatalysis and Prospects of TiO2-Based Photocatalytic DeNOxing the Atmospheric Environment. *Catalysts*. 2018. https://doi.org/10.3390/catal8110553.

(73) Cao, Y.; Li, X.; Bian, Z.; Fuhr, A.; Zhang, D.; Zhu, J. Highly Photocatalytic Activity of Brookite/Rutile TiO2 Nanocrystals with Semi-Embedded Structure. *Appl. Catal. B Environ.* **2016**, *180*, 551–558. https://doi.org/10.1016/j.apcatb.2015.07.003.

(74) Zhang, Q.; Joo, J. B.; Lu, Z.; Dahl, M.; Oliveira, D. Q. L.; Ye, M.; Yin, Y. Self-Assembly and Photocatalysis of Mesoporous TiO2 Nanocrystal Clusters. *Nano Res.* **2011**, *4* (1), 103–114. https://doi.org/10.1007/s12274-010-0058-9.

(75) Ye, M.; Zhang, Q.; Hu, Y.; Ge, J.; Lu, Z.; He, L.; Chen, Z.; Yin, Y. Magnetically Recoverable Core-Shell Nanocomposites with Enhanced Photocatalytic Activity. *Chem. - A Eur. J.* **2010**, *16* (21), 6243–6250. https://doi.org/10.1002/chem.200903516.

(76) Xu, T.; Wu, H.; Cui, K.; Zhao, Q.; Huang, J.; Wei, L.; Ma, Z. Hybrid TiO2/WO3 Nanoparticles Fabricated via a Sol–Gel Process Using Amphiphlic Poly(ε-Caprolactone)-Block-Poly(Acrylic Acid) Diblock Copolymer as Template and Their High Visible Light Photocatalytic Activity. *SN Appl. Sci.* **2019**, *1* (8). https://doi.org/10.1007/s42452-019-0718-7.

(77) Park, H.; Park, Y.; Kim, W.; Choi, W. Surface Modification of TiO2 Photocatalyst for Environmental Applications. *Journal of Photochemistry and Photobiology C: Photochemistry Reviews*. 2013, pp 1–20. https://doi.org/10.1016/j.jphotochemrev.2012.10.001.

(78) Dozzi, M. V.; Prati, L.; Canton, P.; Selli, E. Effects of Gold Nanoparticles Deposition on the Photocatalytic Activity of Titanium Dioxide under Visible Light. *Phys. Chem. Chem. Phys.* **2009**, *11* (33), 7171–7180. https://doi.org/10.1039/b907317e.

(79) Loef, R.; Houtepen, A. J.; Talgorn, E.; Schoonman, J.; Goossens, A. Study of Electronic Defects in CdSe Quantum Dots and Their Involvement in Quantum Dot Solar Cells. *Nano Lett.* **2009**, *9* (2), 856–859. https://doi.org/10.1021/nl803738q.

(80) Loef, R.; Schoonman, J.; Goossens, A. Elucidation of Homojunction Formation in CuInS2

with Impedance Spectroscopy. *J. Appl. Phys.* **2007**, *102* (2). https://doi.org/10.1063/1.2759470.

(81) Su, W. Bin; Wang, J. F.; Chen, H. C.; Wang, W. X.; Zang, G. Z.; Li, C. P. Novel TiO2·WO3 Varistor System. In *Materials Science and Engineering B: Solid-State Materials for Advanced Technology*; 2003; Vol. 99, pp 461–464. https://doi.org/10.1016/S0921-5107(02)00473-7.

(82) Riboni, F.; Bettini, L. G.; Bahnemann, D. W.; Selli, E. WO3-TiO2 vs. TiO2 Photocatalysts: Effect of the W Precursor and Amount on the Photocatalytic Activity of Mixed Oxides. *Catal. Today* **2013**. https://doi.org/10.1016/j.cattod.2013.01.008.

(83) Ren, W.; Ai, Z.; Jia, F.; Zhang, L.; Fan, X.; Zou, Z. Low Temperature Preparation and Visible Light Photocatalytic Activity of Mesoporous Carbon-Doped Crystalline TiO2. *Appl. Catal. B Environ.* **2007**. https://doi.org/10.1016/j.apcatb.2006.06.015.

(84) Grbić, B.; Radić, N.; Stojadinović, S.; Vasilić, R.; Dohčević-Mitrović, Z.; Šaponjić, Z.; Stefanov, P. TiO2/WO3 Photocatalytic Composite Coatings Prepared by Spray Pyrolysis. *Surf. Coatings Technol.* **2014**. https://doi.org/10.1016/j.surfcoat.2014.07.082.

(85) Lee, J. Y.; Jo, W. K. Heterojunction-Based Two-Dimensional N-Doped TiO2/WO3 Composite Architectures for Photocatalytic Treatment of Hazardous Organic Vapor. *J. Hazard. Mater.* **2016**. https://doi.org/10.1016/j.jhazmat.2016.04.012.

(86) Lin, C. F.; Wu, C. H.; Onn, Z. N. Degradation of 4-Chlorophenol in TiO2, WO3, SnO2, TiO2/WO3 and TiO2/SnO2 Systems. *J. Hazard. Mater.* **2008**. https://doi.org/10.1016/j.jhazmat.2007.11.010.

(87) Hao, X.; Li, M.; Zhang, L.; Wang, K.; Liu, C. Photocatalyst TiO2/WO3/GO Nano-Composite with High Efficient Photocatalytic Performance for BPA Degradation under Visible Light and Solar Light Illumination. *J. Ind. Eng. Chem.* **2017**. https://doi.org/10.1016/j.jiec.2017.06.038.

(88) Paula, L. F.; Hofer, M.; Lacerda, V. P. B.; Bahnemann, D. W.; Patrocinio, A. O. T. Unraveling the Photocatalytic Properties of TiO2/WO3 Mixed Oxides. *Photochem. Photobiol. Sci.* **2019**. https://doi.org/10.1039/c9pp00163h.

(89) Georgieva, J.; Valova, E.; Armyanov, S.; Philippidis, N.; Poulios, I.; Sotiropoulos, S. Bi-Component Semiconductor Oxide Photoanodes for the Photoelectrocatalytic Oxidation of Organic Solutes and Vapours: A Short Review with Emphasis to TiO 2-WO 3 Photoanodes. *Journal of Hazardous Materials*. 2012. https://doi.org/10.1016/j.jhazmat.2011.11.069.

(90) Cronemeyer, D. C. Infrared Absorption of Reduced Rutile TiO2 Single Crystals. *Phys. Rev.* **1959**. https://doi.org/10.1103/PhysRev.113.1222.

(91) Leng, W. H.; Zhang, Z.; Zhang, J. Q.; Cao, C. N. Investigation of the Kinetics of a TiO2 Photoelectrocatalytic Reaction Involving Charge Transfer and Recombination through Surface States by Electrochemical Impedance Spectroscopy. *J. Phys. Chem. B* **2005**. https://doi.org/10.1021/jp051821z.

(92) Baram, N.; Ein-eli, Y. Electrochemical Impedance Spectroscopy of Porous TiO 2 for Photocatalytic Applications. *J. Phys. Chem. C* **2010**, *2*, 9781–9790. https://doi.org/10.1021/jp911687w.

(93) He, B. L.; Dong, B.; Li, H. L. Preparation and Electrochemical Properties of Ag-Modified TiO2 Nanotube Anode Material for Lithium-Ion Battery. *Electrochem. commun.* **2007**, *9* (3), 425–430. https://doi.org/10.1016/j.elecom.2006.10.008.

(94) Zhang, H.; Lv, X.; Li, Y.; Wang, Y.; Li, J. P25-Graphene Composite as a High Performance Photocatalyst. *ACS Nano* **2010**, *4* (1), 380–386. https://doi.org/10.1021/nn901221k.